Surface-Enhanced Raman Scattering in BIC-Driven Semiconductor Metasurfaces

Haiyang Hu, Anil Kumar Pal, Alexander Berestennikov, Thomas Weber, Andrei Stefancu, Emiliano Cortés, Stefan A. Maier, and Andreas Tittl*

Semiconductor-based surface-enhanced Raman spectroscopy (SERS) substrates, as a new frontier in the field of SERS, are hindered by their poor electromagnetic field confinement and weak light-matter interaction. Metasurfaces, a class of 2D artificial materials based on the electromagnetic design of nanophotonic resonators, enable strong electromagnetic field enhancement and optical absorption engineering for a wide range of semiconductors. However, the engineering of semiconductor substrates into metasurfaces for improving SERS activity remains underexplored. Here, an improved SERS metasurface platform is developed that leverages the combination of titanium oxide (TiO_2) and the emerging physical concept of optical bound states in the continuum (BICs) to boost the Raman emission. Moreover, fine-tuning of BIC-assisted resonant absorption offers a pathway for maximizing the photoinduced charge transfer effect (PICT) in SERS. High values of BIC-assisted electric field enhancement ($|E/E_0|^2 \approx 10^3$) are achieved, challenging the preconception of weak electromagnetic (EM) field enhancement on semiconductor SERS substrates. The BIC-assisted TiO_2 metasurface platform offers a new dimension in spectrally-tunable SERS with earth-abundant and bio-compatible semiconductor materials, beyond the traditional plasmonic ones.

H. Hu, A. K. Pal, A. Berestennikov, T. Weber, A. Stefancu, E. Cortés, A. Tittl
Chair in Hybrid Nanosystems
Nanoinstitute Munich
Faculty of Physics
Ludwig-Maximilians-Universität München
80539 München, Germany
E-mail: andreas.tittl@physik.uni-muenchen.de
S. A. Maier
School of Physics and Astronomy
Monash University Clayton Campus
Melbourne, Victoria 3800, Australia
S. A. Maier
The Blackett Laboratory
Department of Physics
Imperial College London
London SW7 2AZ, UK

The ORCID identification number(s) for the author(s) of this article can be found under https://doi.org/10.1002/adom.202302812

1. Introduction

Surface-enhanced Raman spectroscopy (SERS) is a highly sensitive, chemically specific, and non-destructive analytical technique that has garnered significant attention in the fields of biophysics, chemistry, and medical diagnostics.[1–5] The SERS substrate is at the core of SERS-based technologies, providing large Raman enhancement factors through two independent mechanisms: electromagnetic (EM) and chemical (CM).[2,6–8] So far, noble metals such as Au, Ag, and Cu have played a dominant role in SERS applications due to their ability to quench fluorescence and enhance the EM fields through plasmon resonances, achieving ultrasensitive and even single-molecule-level SERS detection.[9–13] However, there are some disadvantages for noble metal SERS substrates such as high cost, poor chemical and thermal stability, lack of uniformity and biocompatibility, low SERS signal reproducibility, and poor selective recognition ability for probe molecules.[9,14,15] Semiconductor SERS substrates are a promising alternative to metals due to their better chemical stability and biocompatibility.[16] Semiconductor materials are capable of manipulating light at the nanoscale (using optical absorption engineering, light trapping by total internal reflection, etc.),[17,18] and they allow for straightforward surface modification with a diverse range of functional groups (-NH_2, -COO-, -PO_4^{3-}, -SH, etc.),[2] which have significantly broadened SERS applications across various fields.[4,9,15,19,20] In particular, semiconductor SERS substrates benefiting from photoinduced charge transfer (PICT),[9,15,21] have also demonstrated great potential for detecting target molecules in complex environments and monitoring interfacial chemical reactions with high sensitivity, making them valuable tools in the fields of biophysics, chemistry, and medical diagnostics research.[22]

However, compared to noble metals, semiconductor substrates generally have a poorer limit of detection, which can be attributed to weaker EM field enhancement and light-matter interactions.[14,23–25] Therefore, it is crucial to explore strategies to improve the SERS performance of semiconductor substrates.[26] To this end, several methods have been reported to enhance the EM field and light-matter interaction. Common approaches based on Mie resonances are to

**ADVANCED
SCIENCE NEWS**

www.advancedsciencenews.com

**ADVANCED
OPTICAL
MATERIALS**
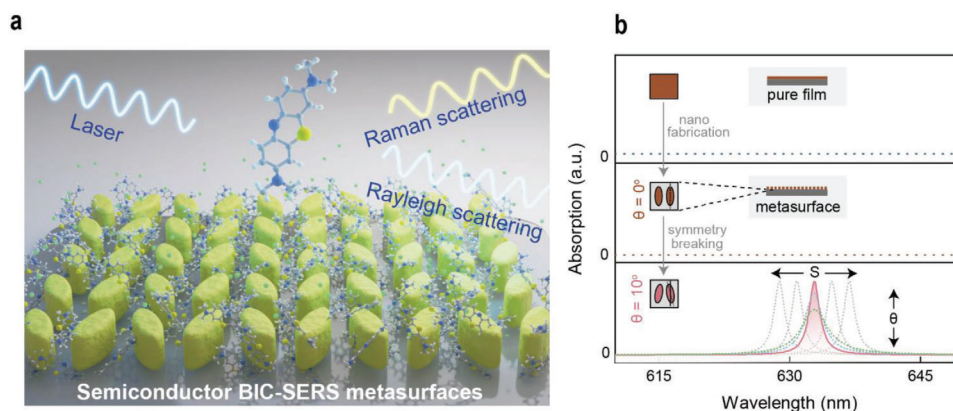
www.advopticalmat.de

Figure 1. BIC-driven TiO$_2$ semiconductor SERS metasurface. a) Schematic of the TiO$_2$-based BIC metasurface platform for SERS applications. b) Illustration of BIC-assisted absorption enhancement and spectral tunability. The simulated absorbance spectra for the pure TiO$_2$ film (top), BIC-assisted TiO$_2$ metasurfaces with the symmetrical geometry (middle), and asymmetrical geometry ($\theta = 10°$) as an example (bottom). The absorbance of the metasurface can be enhanced with the excitation of quasi-BIC resonances in asymmetrical geometry. This can be further spectrally tailored through the S (scaling factor), and the amplitudes can additionally be tuned by adjusting the degree of asymmetry factor (θ).

synthesize semiconductor nanospheres to trap light,[27] or assemble homogeneous spheres to form 2D arrays or 3D colloidal crystals.[28] Alternatively, semiconductor doping has also been applied to generate surface plasmon resonance (SPR), which inevitably introduces enormous optical loss.[2,29] However, these methods have not fully harnessed one of the most distinctive advantages of semiconductors: their optical engineering capabilities.[2,30]

Metasurfaces constructed from 2D subwavelength arrays of semiconductor nanostructures have shown tremendous potential for enhancing light-matter interaction at the nanoscale.[2,31–35] In particular, metasurfaces underpinned by the physics of bound states in the continuum (BIC) have seen a surging interest due to their strong light confinement and remarkable enhancement of electromagnetic fields,[36,37] stimulating applications across diverse fields, including nanoscale lasing,[38,39] biomolecular sensing,[40–42] and nonlinear photonics.[43,44] Hence, BIC-assisted metasurfaces serve as an ideal toolkit for light manipulation in semiconductor SERS substrates (**Figure 1a**), which, to the best of our knowledge, have not yet been realized.

Here, we demonstrate BIC-driven semiconductor metasurfaces as a new platform for high-sensitivity SERS. Through precise nanophotonic engineering of quasi-BIC resonances in the TiO$_2$ BIC system, we successfully enhance both the PICT effect (chemical mechanism) and the EM field confinement (physical mechanism) of SERS. Significantly, the integration of metasurface nano-engineering techniques with BIC physics offers a versatile approach applicable to a wide range of semiconductor SERS substrate materials (with low intrinsic losses), which can be adapted to diverse molecules like methylene blue (MB), Rhodamine 6G, and adenine.[9,15,45] This synergistic combination leverages the benefits of nanoscale light manipulation (metasurface) and the remarkable chemical effects empowered by photoinduced charge transfer (semiconductor), thereby optimizing the SERS performance of these substrates.

2. Results and Discussion

Conceptually, a BIC is a localized state existing in a continuum of radiative modes.[36,46] This phenomenon originally appeared in quantum mechanics and has later been applied to many other areas of physics where resonant behavior is prevalent.[47] A true BIC, with an infinite value of the quality factor (Q factor, defined as the resonance position divided by the line width), can be explained by vanishing coupling constants with all radiation channels.

One way of making BICs usable in practical nanophotonic systems is to design symmetry-protected metasurfaces, where the coupling constants to the radiation continuum are tailored using structural asymmetry within the metasurface unit cell, leading to the formation of quasi-BIC modes accessible from the far field.[36] The narrow quasi-BIC could be a drawback from the perspective of scaling the EM enhancement of the Stokes-shifted field, however, it offers several advantages for the SERS application. A key advantage of symmetry-protected BICs is their ability to accurately control the resonance position (Figure 1b). This attribute is particularly crucial for semiconductor SERS platforms, since matching the quasi-BIC resonance to the laser wavelength can significantly enhance the SERS sensitivity.

2.1. Numerical Investigation of TiO$_2$ BIC Metasurfaces

We implemented metasurfaces with two different geometries (two ellipses and hole-in-disk) for our BIC metasurfaces designs (**Figure 2a,b**). As introduced previously, for semiconductor SERS applications, both the enhanced absorption of the incident light source leading to the substrate-molecule PICT effect, and the inherent strong electric field enhancement of the nanomaterial are vital to the amplification of the Raman signal. Hence, in our simulation, we evaluate the absorption and electric field enhancement for these two metasurface geometries.

As mentioned above, a true BIC is a mathematical concept characterized by infinite quality factor and vanishing spectral
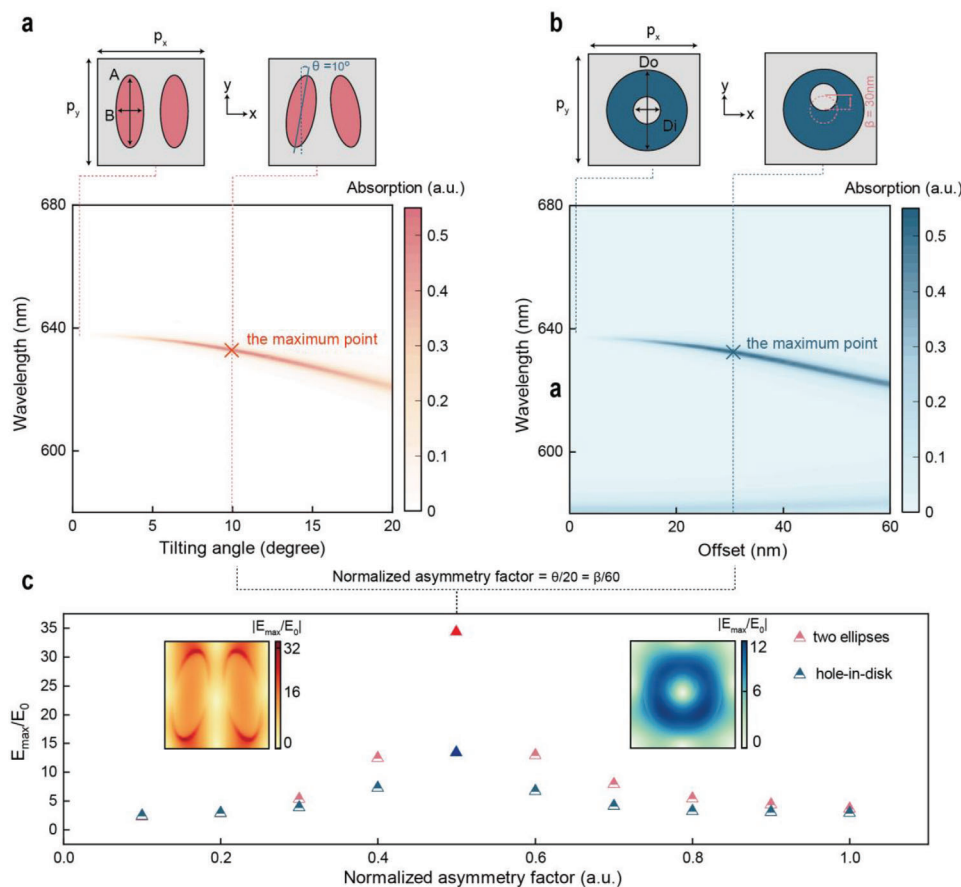
ADVANCED
SCIENCE NEWS

www.advancedsciencenews.com

ADVANCED
OPTICAL
MATERIALS

www.advopticalmat.de

Figure 2. Numerical design of semiconductor SERS metasurfaces and their far/near field properties. a) Top: Sketch of a BIC unit cell with the two ellipses geometry (A, B, P_x, and P_y will scale linearly according to scaling factor S). The geometrical parameters of the unit cell are A = 302 nm, B = 115 nm, P_x = P_y = 366 nm ($S = 1$). The symmetry can be broken by tuning the tilting angle (θ). Bottom: Color-coded simulated absorbance maps of TiO$_2$ metasurfaces as a function of tilting angle θ and wavelength. b) Top: Sketch of the unit cell with hole-in-disk geometry (Di, Do, P_x, and P_y will scale linearly according to scaling factor S). The geometrical parameters of the unit cell are Di = 90 nm, Do = 263 nm, P_x = P_y = 366 nm ($S = 1$). Here we can shift the hole along the y-axis (β) to break the symmetry. Bottom: Color-coded simulated absorbance maps of metasurfaces as a function of offset value (β) and wavelength. c) The simulated electric field enhancement of metasurfaces with different geometries (two ellipses, and hole-in-disk) under different asymmetry factors. For ellipses and hole-in-disk geometries, we normalize the asymmetry parameter θ and β as follows, normalized asymmetry factor = θ / 20 = β / 60. We set the tuning range of θ from 0 to 20 degrees, and β from 0 to 60 nm, which are consistent with the above simulated absorbance maps. Inset: The electric near field at the resonance frequency for unit cells (two ellipses, and hole-in-disk) of TiO$_2$ metasurfaces, corresponding to maximum absorption, and field enhancement.

line width. In practice, true BICs can be converted to quasi-BICs with finite resonance width by breaking the in-plane inversion symmetry within the unit cell, allowing the resonant mode to be excited from the far field. For the unit cell with two ellipses, the symmetry breaking can be achieved by tilting the ellipses at an angle θ with respect to each other. In the hole-in-disk geometry, the symmetry is broken by shifting the hole from the center along the y-axis by a specific value (β).

Through the quasi-BIC resonance, we can achieve a significant enhancement in absorption after breaking the C_2^Z symmetry in the metasurfaces. The absorbance spectrum is calculated from the simulated reflectance (R) and transmittance (T) spectra ($A = 1 - R - T$). Here, we emphasize one of the most important advantages of BIC metasurfaces in SERS applications, namely

that the light confinement at the interface (characterized by absorbance) can be maximized through tuning the asymmetry parameter. Specifically, we used numerical simulations for calculating absorbance maps of TiO$_2$ metasurfaces with different geometries (two ellipses and hole-in-disk) as a function of the asymmetry parameters θ and β. The absorbance enhancement of the quasi-BIC resonances is found to be strongly dependent on the asymmetry parameter, reaching maximum magnitudes at specific values ($\theta = 10$ degrees, and $\beta = 30$ nm, respectively), as determined by the critical coupling condition explained by the temporal coupled-mode theory. In brief, the BIC-enabled semiconductor SERS metasurface platform can be described as a single-mode cavity with two mirror-symmetric ports, where the interaction between the far-field and the cavity mode at each port is determined by the coupling rate κ, which can be derived from the radiative

**ADVANCED
SCIENCE NEWS**

www.advancedsciencenews.com

**ADVANCED
OPTICAL
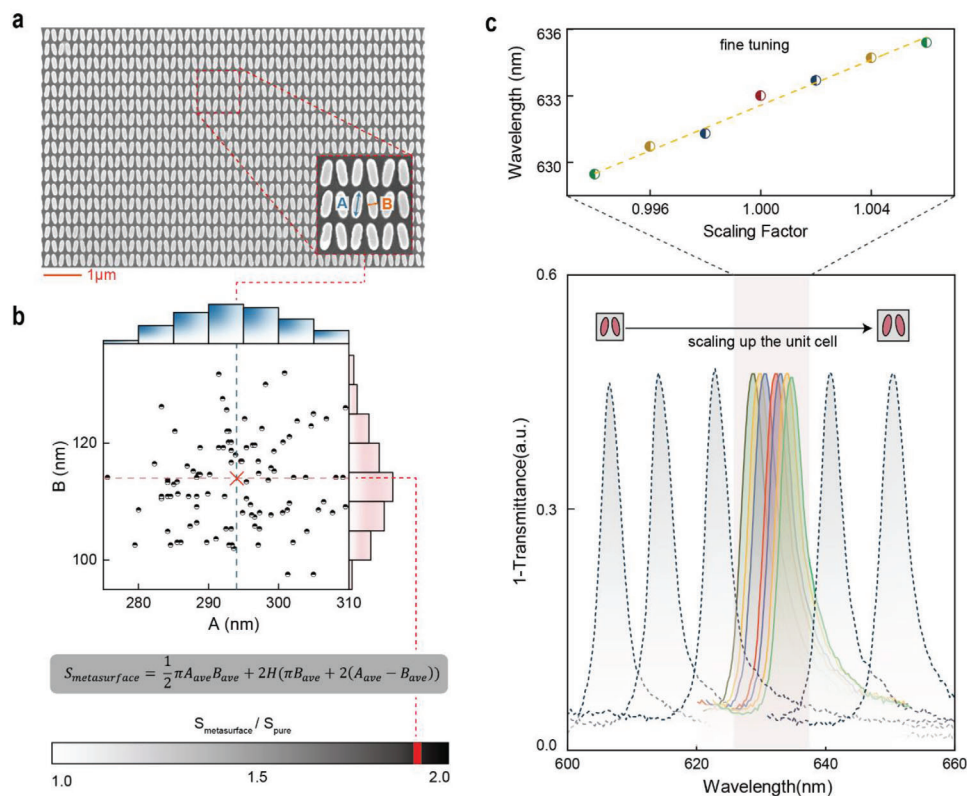MATERIALS**

www.advopticalmat.de

Figure 3. Experimental metasurface fabrication and spectral tuning. a) SEM images of experimental metasurfaces with two ellipse geometry (scaling factor $S = 1$). b) Statistical measurements of the length of long and short axes (A and B) of the ellipses in different unit cells (100 in counting), where average values for A and B are 294 ± 7.51 and 114 ± 7.62 nm, respectively. The $\pm$ notation indicates the standard deviations associated with the average dimensions of A and B. The surface area of a single unit cell ($S_{metasurface}$) is calculated based on these values according to the proximate formula shown in the figure, which is compared with the surface area of the unstructured pure film (S_{pure}) with the same size as the periodic of the single unit cell (366 × 366 nm), resulting in a factor of 1.9 ($S_{metasurface}/S_{pure}$). c) Measured transmittance spectra for metasurfaces with different scaling factors (0.994 to 1.006 for fine tuning). Both the dashed and solid lines are measured spectra.

decay rate γ_{rad}. Additionally, an intrinsic decay rate γ_{int} accounts for the energy loss through material absorption, and the far-field absorbance can be calculated according to:

$$A = \frac{2\,\gamma_{int}\,\gamma_{rad}}{\left(\gamma_{int} + \gamma_{rad}\right)^2} \tag{1}$$

which reaches its maximum value when the intrinsic decay rate γ_{int} is equal to the radiative decay rate γ_{rad}, referring to the critical coupling condition.[48]

Although both geometries can achieve the maximum absorbance magnitude (A = 0.5) under the critical coupling condition, they present different near-field EM enhancements, which is also an important aspect for SERS.[49] It can be clearly seen that the unit cell with two ellipses geometry exhibited stronger electric field enhancement ($|E/E_0| = 32$) than the hole-in-disk geometry ($|E/E_0| = 12$) even though both of them operate at the critical coupling condition (Figure 2c). It's worth noting that semiconductor SERS substrates typically rely on the chemical mechanism (PICT) to amplify the Raman signal, but often suffer from extremely weak EM enhancement.[14,23,24] Here, our semiconductor metasurfaces, empowered by the BIC resonances, allow for

strong electric field enhancement. Conducting the SERS experiment on these metasurfaces of different geometries could deepen our understanding of how the BIC metasurface geometry affects SERS performance.

2.2. Experimental Fabrication of TiO$_2$-Based Metasurfaces

While bottom-up methods can provide scalable production and produce a wide variety of nanostructures, considering the importance of precise control over the shape and spatial distribution of all metasurface elements, we employed top-down nanofabrication. TiO$_2$ thin films with a thickness of 140 nm were fabricated by sputter deposition, followed by high-resolution electron beam lithography and anisotropic reactive ion etching (see Methods section for details).

We experimentally implemented the metasurfaces designs composed of two ellipses (**Figure 3a**) and hole-in-disk geometries (Figure S1, Supporting Information). Here, we took two ellipses metasurfaces as an example to confirm their fabrication quality using electron microscopy (Figure 3a). We performed statistical measurements on the long and short axes (A and B) of 100 unit cells, obtaining average values of ±294 and ±144 nm, respectively
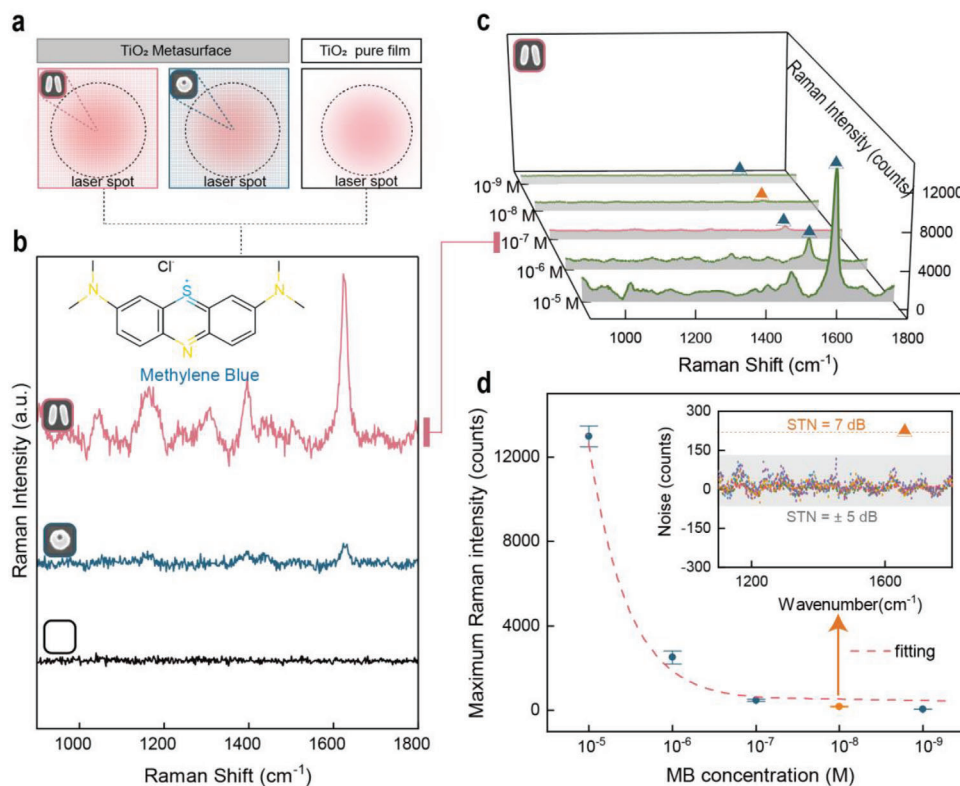
Figure 4. Raman spectra of methylene blue on the BIC-assisted semiconductor SERS metasurface. a) Schematic layout of the laser illuminating on the TiO$_2$ BIC metasurfaces (two ellipses, and hole-in-disk geometries), and the pure TiO$_2$ film, where BIC metasurfaces pattern (32×32 μm^2) can be successfully excited by a laser (14 μm in diameter). b) Raman spectra for MB were measured on the BIC metasurfaces with different geometries (two ellipses, and a hole-in-disk), and on the pure TiO$_2$ film, where the concentration of MB solution is 10^{-7} M, and the excitation laser wavelength is 633 nm. c) The Raman spectra for MB at different concentrations (10^{-5} to 10^{-9} M) on the BIC-assisted TiO$_2$ semiconductor SERS substrate with two ellipses geometry. d) The maximum Raman signal of MB (at 1624 cm^{-1}) at different concentrations measured on the metasurfaces with two ellipses geometry (data extracted from Figure 4c), and the analysis of the signal-to-noise ratio (inset). The noise signal background is gathered from the unstructured TiO$_2$ film under the same settings.

(Figure 3b). We increased the effective surface area of semiconductor metasurfaces by approximately two times compared to the non-structured pure TiO$_2$ film, which provides a greater active contact surface area for analyte molecules to form surface complexes and generate stronger Raman signal.[45]

The presence of quasi-BIC resonances has been confirmed through white light transmittance measurements (see the Methods section). We experimentally demonstrate broad spectral tunability of the semiconductor BIC metasurfaces by scaling the size of the unit cell (S), which enabled us to control the position of the quasi-BIC resonance throughout the whole visible spectrum (Figure 3c), and cover several widely used Raman laser sources (532, 633, and 785 nm). Fine-tuning the S factor around the target laser wavelength (633 nm here) ensured that we could precisely excite the quasi-BIC resonance. We applied the temporal coupled-mode theory (TCMT) model to fit the experimental transmittance spectrum,[50] which characterizes the spectral mode energy density and is directly related to the enhancement of light-matter interaction.[51]

Matching the excitation wavelength to the semiconductor substrate absorption has been a long-standing challenge for SERS semiconductor substrates,[3] which has now been experimentally achieved in our semiconductor BIC metasurfaces. Additionally,

when the laser wavelength matches the molecular absorption resonance, the Raman signal can be amplified by several orders of magnitude due to the resonant Raman effect (as discussed in the following section).[49]

2.3. BIC-Assisted Semiconductor SERS Metasurface

We utilized MB as a test molecule for SERS investigations together with a 633 nm laser as the excitation source (see Methods). Taking advantage of the high spectral tunability of our semiconductor SERS substrate, we engineered the resonance position of metasurfaces with different meta-units (two ellipses, and a hole-in-disk) to match the pump wavelength (633 nm) by finely tuning the S factor (discussed in Figure 3). The target BIC metasurfaces pattern with the size of 33×33 μm^2 is illuminated by the excitation laser with a spot size around 14 μm in diameter passing through a 20 X water-immersed objective, which ensured the successful excitation of quasi-BIC resonance (**Figure 4**a). It is well known that in SERS applications, the excited molecules can emit also fluorescence in addition to the Raman emission. This is particularly important in semiconductor SERS substrates which, unlike metals, do not quench the fluorescence emission.[26] Hence,

**ADVANCED
SCIENCE NEWS**

www.advancedsciencenews.com

**ADVANCED
OPTICAL
MATERIALS**

www.advopticalmat.de

in this research, we employed an automated algorithm for fluorescence removal based on modified multi-polynomial fitting (see Methods, and Figure S2a,b, Supporting Information).[52]

To better understand the SERS application of the BIC-assisted semiconductor TiO$_2$ metasurfaces, we compared the SERS enhancement on the two ellipses and hole-in-disk metasurfaces. Specifically, for the same MB concentration (10^{-7} M), the semiconductor BIC metasurface with two ellipses exhibited a SERS signal approximately seven times higher than that of hole-in-disk geometry, which is attributed to the higher EM field enhancement associated with the two ellipses geometry (discussed in next section) in the vicinity of BIC metasurfaces. Outstanding SERS enhancement by the BIC metasurfaces was observed when we compared it with the non-patterned pure TiO$_2$ film where no appreciable Raman scattering was detected, thereby proving the fundamental advantages offered by the BIC metasurfaces engineering technique for semiconductor SERS substrates (Figure 4b). Additionally, to confirm that the SERS enhancement is indeed induced by the BIC resonance, we deactivate the resonance by rotating the BIC metasurfaces by 90°, which consequently resulted in no SERS enhancement (Figure S2c, Supporting Information), despite having the same surface area (i.e., equal amount of molecules interacting with the platform).

The SERS detection sensitivity of the two ellipses semiconductor BIC metasurfaces was further investigated by performing Raman measurements at different MB concentrations (10^{-5} to 10^{-9} M). It can be clearly seen that the Raman signal intensity decreased sharply with decreasing MB concentration (Figure 4c). The detection sensitivity for MB on our BIC-assisted semiconductor SERS metasurfaces was 10^{-8} M, which was evaluated from the signal-to-noise ratio, in accordance with IUPAC recommendations.[53] We estimated the detection sensitivity of our SERS metasurfaces by considering both the processing error induced by mathematically removing the autofluorescence background signals (see Methods) and the noise level associated with our experiments, which includes detector noise, source stability, and optical alignment.[41] Specifically, we captured a total of $n = 5$ reference Raman measurements, using BIC metasurfaces that mismatched the excitation laser (633 nm) and proceeded with the same mathematical background noise removal treatment. Based on the obtained Raman spectra, we calculated the standard deviation for each reference Raman spectrum and obtained the average value for the amplitude of the noise background (see Methods). The signal-to-noise ratio (STN, in dB) was calculated according to the following formula (Equation (2)), where A_{signal} is the amplitude of the specified Raman signal (1624 cm^{-1}) mode, and A_{noise} is the amplitude of background noise, which can be obtained as described earlier.

$$STN = 10 \times log_{10}\left(A_{signal}/A_{noise}\right) \quad (2)$$

The calculated STN of the Raman mode (1624 cm^{-1}) with maximum amplitude is approximately 7 dB (Figure 4d), which exceeds the common threshold for minimum acceptable SNR (3 dB).[54]

In summary, we have experimentally demonstrated significant SERS enhancement of MB on our BIC-assisted semiconductor metasurfaces, achieving detection sensitivity of 10^{-8} M which is higher than the reported TiO$_2$ semiconductor SERS sub-

strates for MB sensing (10^{-6} M).[23,24] To deepen our understanding of mechanisms underlying the SERS enhancement achieved through BIC-assisted semiconductor metasurfaces, we will discuss the chemical and EM enhancement mechanisms in the following section.

2.4. Hybrid Effects on BIC-Assisted Semiconductor SERS Metasurface

Enhancing the photoinduced charge transfer (PICT) effect between semiconductors and molecules is an established general strategy for achieving a high enhancement on semiconductor SERS substrates.[55] When the molecules are bound to the semiconductor surface by weak covalent bonds, the charge can be transferred across the interface between the semiconductor and molecule, which can generate strong Raman enhancement if the excitation frequency resonates with the PICT transition.[2,21,23,56,57] Specifically, when the energy levels of the semiconductor are coupled with the absorbed molecules, the charge can be transferred from the valence band states ($|\underline{V}\rangle$) of the semiconductor to the molecular excited states ($|\underline{K}\rangle$) via the transition moment, μ_{VK}, or from the molecular ground state ($|I\rangle$) to the conduction band states ($|C\rangle$) of the semiconductor via the transition moment, μ_{IC}, which can be further enhanced through borrowed intensity either from exciton transition μ_{VC} or molecular transitions μ_{IK}, through the Herzberg-Teller coupling term (h_{CK} or h_{VI}), as shown in **Figure 5a**.[21,23]

As discussed above, matching the excitation laser with the molecular resonance is pivotal for achieving high PICT rates, and consequently high SERS enhancement factors, typically by 3–4 orders of magnitude.[2] This enhancement can be further amplified by absorption engineering in tailored SERS substrates. Due to the diversity of molecular analytes, conventional semiconductor SERS substrates face challenges in maximizing the absorption of the excitation visible laser source which matches the molecular resonance. To address this limitation, the absorption of the two-ellipse TiO$_2$ metasurface can be optimized to its maximum value by precisely tailoring the radiation loss via tuning the asymmetry factor (θ) to match intrinsic losses, thus satisfying the critical coupling condition.[58] Tailoring our BIC resonance to match the molecular resonance in the UV region poses challenges due to the intrinsic loss characteristics of TiO$_2$ in that range. Therefore, we have strategically targeted the visible region, ensuring alignment with the corresponding molecules and effectively leveraging the advantageous properties of TiO$_2$ BIC metasurfaces.

We obtained the maximum absorption on the TiO$_2$ metasurface for $\theta = 10°$ (Figure 5b). After successfully achieving the maximum absorption enhancement of TiO$_2$ metasurface at the molecular resonance position, the charge-transfer resonance and molecular resonance can couple to each other by the Herzberg-Teller coupling constant,[2] which can further boost the PICT effect and provide stronger SERS activity of our BIC-assisted semiconductor SERS metasurface.

Even though the chemical mechanism (PICT) plays an important role in semiconductor SERS technologies, here, we also emphasize the importance of the physical mechanism brought by BIC metasurfaces to the field of semiconductor SERS substrates.
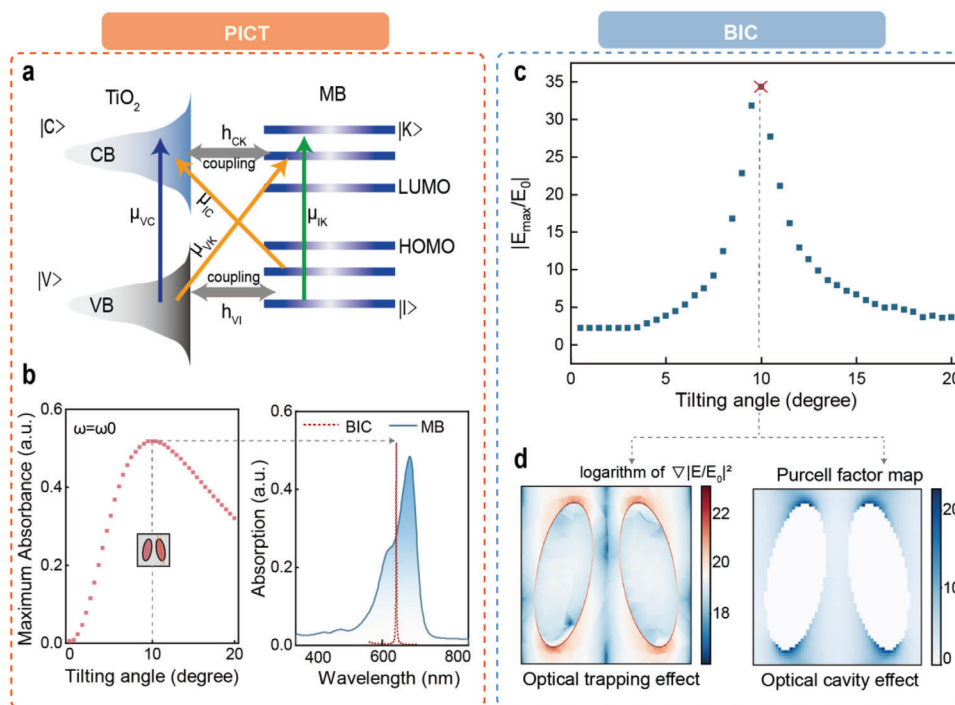
Figure 5. Hybrid effect of BIC-assisted semiconductor SERS metasurface. a) Schematic PICT transition in the semiconductor-molecule system. b) Left: Simulations of absorbance at the resonance ($\omega = \omega_0$) for the TiO$_2$ BIC metasurfaces (two ellipses geometry) at different tilting angles ($\theta = 1$–20°). Right: Enhanced absorption of TiO$_2$ BIC metasurfaces ($\theta = 10°$), aligned with the absorption of MB (10^{-3} M). c) Simulations of the electric field enhancement in TiO$_2$ BIC metasurfaces at various tilting angles ($\theta = 1$–20°), where the maximum field enhancement is achieved at $\theta = 10°$, satisfying the critical coupling condition (radiation loss equals intrinsic loss). d) Left: The logarithm of the gradient of the squared electric field enhancement, based on simulation results, which can be used to estimate the optical trapping effect on the MB molecular. Right: Map of the Purcell factor values for a single unit cell to evaluate the enhanced light-matter interaction in the BIC nanocavity.

Because the SERS signal is proportional to the enhancement of the EM field,[59] achieving high EM field enhancements has been a long-standing challenge in the semiconductor SERS community. As already described above, strong EM field enhancement can be achieved by engineering the semiconductor TiO$_2$ substrate into a BIC metasurface, thereby benefiting from strong light localization provided by the BIC resonances. Our BIC-driven TiO$_2$ substrate produces maximum EM field enhancement at $\theta = 10°$ (Figure 5c), where |E| represents the absolute magnitude of the local electric field with the metasurface, and |E$_0$| represents the incident field without structure. The highest electric field enhancement (|E|/|E$_0$|) is found to be around 35 at the resonance frequency. Additionally, the large gradient of the squared electrical field $F_{grad} \propto \nabla |\vec{E}(r)|^2$ at the hot spots region (Figure 5d) suggests a possible molecule trapping effect.[60] The contribution of enhanced EM field to the amplification of radiative spontaneous emission can be explained by the Purcell effect as given below,[51,61]

$$F_p = \frac{3}{4\pi^2} \left(\frac{\lambda_c}{n_c} \right)^3 \left(\frac{Q}{V_{eff}} \right) \tag{3}$$

where λ_c is the resonance wavelength, n_c is the refractive index of the medium, Q is the resonance quality factor, and V_{eff} is the effective mode volume. This is the classical definition of the Purcell

factor, however, V_{eff} is not straightforward to define and evaluate for open optical systems.[61,62]

Alternatively, the Purcell factor can also be defined as the change of the total radiated power at the frequency of the emitter.[63,64] The method is based on numerical simulations of the power radiated by an active dipole coupled to the resonators (P_{rad}) divided by the radiated power of the same emitter in free space ($P_{0,rad}$) (see Methods section for calculation details)

$$F_p = \frac{P_{rad}}{P_{0,\,rad}} \tag{4}$$

Figure 5d shows the Purcell factor map in a unit cell at the resonant frequency. Comparing the values of the Purcell factor, one can clearly see that the Purcell factor around the vertices of the ellipses is much higher ($F_p \sim 20$). Hence, through mapping the Purcell factor over the whole unit cell region, we can clearly observe larger Purcell factors around the hot spot region of the BIC resonators, illustrating the strong capability of enhancing the Raman signal in this area, which highlights the active role of BIC resonance in amplifying Raman activity.

3. Conclusion

We have developed TiO$_2$-based semiconductor SERS metasurfaces, and demonstrated that the synergistic integration of

2302812 (7 of 9)

semiconductor materials and BIC-resonant photonic metasurfaces offers tremendous potential for advanced sensing and detection applications. We challenge the preconception that the conventional semiconductor SERS substrates suffer from inefficient EM field enhancement, by showing high electric field enhancement ($|E/E_0|^2 \approx 10^3$) on our BIC platform. Additionally, due to the possibility of fine-tuning the BIC resonance across a wide range, it is easy to match it with the absorption wavelength of the analyzed molecule resulting in the enhanced PICT effect. Based on our BIC-assisted semiconductor SERS metasurfaces, we demonstrate a detection efficiency for the molecule MB at 10^{-8} M, two-fold higher than the one reported for TiO$_2$ semiconductor SERS substrates (10^{-6} M).[23,24] Finally, our BIC-assisted semiconductor SERS metasurfaces platform circumvents the long-standing drawbacks of many semiconductor SERS substrates, such as the poor spectral tunability of light absorption, weak electromagnetic field enhancement, and lack of strong light-matter interaction, and shows that improved SERS activity can be extended to multiple sensing systems with different semiconductor substrates and analytes.

4. Experimental Section

Numerical Simulation: Simulations were performed using the finite-element frequency-domain Maxwell solver included in CST Studio Suite 2021, and Lumerical FDTD software taking into account the experimentally measured optical constants of TiO$_2$. The default value (n = 1.5) implemented in CST Studio Suite for the SiO$_2$ substrate was utilized. The optical far-field absorbance in an aqueous environment was calculated via $A = 1 - T - R$, where transmittance (T) and reflectance (R) spectra were simulated under linearly polarized normally incident illumination. The E-field monitor with the corresponding eigenfrequency was added for the electric near-field simulation. The Purcell factor was calculated using the COMSOL Multiphysics package. A dipole source located along the y-axis was moved along the central unit cell of the finite (15 × 15 unit cells) BIC metasurface. The Purcell factor was calculated as the ratio of the integral power flux through the sphere surrounding the dipole in the presence of a metasurface and in a vacuum.

Materials: Polymethyl methacrylate (PMMA), a high-resolution positive resist for direct write e-beam, was applied. Specifically, PMMA was chosen with 950 000 (950k) molecular weight (MW) resins in anisole with a concentration of 4% (A4), sourced from AllRESIST. The developer formulation was a blend of methyl isobutyl ketone (MIBK) and isopropyl alcohol (IPA) with a ratio of 1:3 (Sigma–Aldrich). The methylene blue is sourced from Sigma–Aldrich.

Nanofabrication of Metasurface: Sputter deposition (Angstrom) was applied to produce TiO$_2$ (140 nm) films. Before the electron-beam lithography step, the sample was spin-coated with a layer of photoresist (PMMA 950K A4) followed by spin-coating a conducting layer (ESpacer 300Z). The unit cells with different geometries (two ellipses, and hole-in-disk) were patterned with electron-beam lithography (Reith Eline Plus) with an acceleration voltage of 20 kV and a 15 μm aperture. The samples were transferred to a 3:1 MIBK: IPA solution for developing for 135s, followed by the deposition of a 50 nm chrome layer as the hard mask. Lift-off was conducted in Microposit Remover 1165 overnight at 80 °C, followed by reactive ion dry etching in an RCP-RIE system with a SF$_6$/Ar plasma for 135s. The chrome hard mask was removed through wet etching with chromium etchant (Sigma–Aldrich).

Optical Measurements: Transmittance measurements of the fabricated metasurface samples were carried out with a WiTec optical microscope comprising a water immersion objective (20X, NA = 0.5, Zeiss, Germany), where the metasurfaces were immersed in methylene blue solution

(10^{-7} M, 150 μL) illuminated by a Thorlabs OSL2 white light source with linear polarization.

SERS Measurement: Raman measurements were carried out with the WiTec optical microscope equipped with three linear polarized CW lasers 532, 633, and 785 nm. As shown in Figure S4 (Supporting Information), the sample was aligned to ensure the electric field was polarized along the short axis of the ellipses, which is referred to as x polarization excitation. When the sample was rotated by 90°, the electric field was polarized along the long axis of the ellipses (y polarization), where the quasi-BIC resonance was not excited. The TiO$_2$ BIC metasurfaces were immersed in 150 μL of methylene blue (Sigma–Aldrich) water solution (10^{-7} M) illuminated with 633 nm laser (spot size of 14 μm in diameter) through a water immersion objective (20X, NA = 0.5, Zeiss, Germany) on the corresponding metasurfaces pattern (33 × 33 μm^2) with matching resonance wavelength. For spectra acquisition, the incident power on the sample was set to 1 mW with a dwell time of 50 s. The Raman signal was computationally derived from the fluorescence background through the literature-reported subtraction algorithm, where modified multi-polynomial fitting was applied, which suppresses the undesirable artificial peaks that might occur in polynomial fitting by taking the effects of noise level and peak contribution into account.

Supporting Information

Supporting Information is available from the Wiley Online Library or from the author.

Conflict of Interest

The authors declare no conflict of interest.

Data Availability Statement

The data that support the findings of this study are available from the corresponding author upon reasonable request.

**ADVANCED
SCIENCE NEWS**

www.advancedsciencenews.com

**ADVANCED
OPTICAL
MATERIALS**

www.advopticalmat.de

[1] J. F. Li, Y. F. Huang, Y. Ding, Z. L. Yang, S. B. Li, X. S. Zhou, F. R. Fan, W. Zhang, Z. Y. Zhou, D. Y. Wu, B. Ren, Z. L. Wang, Z. Q. Tian, *Nature* **2010**, *464*, 392.

[2] I. Alessandri, J. R. Lombardi, *Chem. Rev.* **2016**, *116*, 14921.

[3] F. Sun, H. C. Hung, A. Sinclair, P. Zhang, T. Bai, D. D. Galvan, P. Jain, B. Li, S. Jiang, Q. Yu, *Nat. Commun.* **2016**, *7*, 13437.

[4] R. Haldavnekar, K. Venkatakrishnan, B. Tan, *Nat. Commun.* **2018**, *9*, 3065.

[5] M. Arabi, A. Ostovan, Y. Wang, R. Mei, L. Fu, J. Li, X. Wang, L. Chen, *Nat. Commun.* **2022**, *13*, 5757.

[6] A. Otto, *J. Raman Spectrosc.* **2005**, *36*, 497.

[7] E. C. Le Ru, E. Blackie, M. Meyer, P. G. Etchegoint, *J. Phys. Chem. C* **2007**, *111*, 13794.

[8] E. C. Le Ru, P. G. Etchegoin, M. Meyer, *J. Phys. Chem. C* **2006**, *125*, 20.

[9] Z. Zheng, S. Cong, W. Gong, J. Xuan, G. Li, W. Lu, F. Geng, Z. Zhao, *Nat. Commun.* **2017**, *8*, 1993.

[10] B. W. Lin, Y. H. Tai, Y. C. Lee, D. Xing, H. C. Lin, H. Yamahara, Y. L. Ho, H. Tabata, H. Daiguji, J. J. Delaunay, *Appl. Phys. Lett.* **2022**, *120*, 5.

[11] Z. Wang, Y. L. Ho, T. Cao, T. Yatsui, J. J. Delaunay, *Adv. Funct. Mater.* **2021**, *31*, 2102183.

[12] J. Zhu, Y. Xie, Y. Gao, In Emergent Micro- and Nanomaterials for Optical, Infrared, and Terahertz Applications, CRC Press, **2022**.

[13] X. Yao, S. Jiang, S. Luo, B. W. Liu, T. X. Huang, S. Hu, J. Zhu, X. Wang, B. Ren, *ACS Appl. Mater. Interfaces* **2020**, *12*, 36505.

[14] S. Cong, S. Yuan, Z. Chen, J. Hou, M. Yang, Y. Su, Y. Zhang, L. Li, Q. Li, F. Geng, Z. Zhao, *Nat. Commun.* **2015**, *6*, 7800.

[15] X. Wang, L. Guo, *Angew. Chem.* **2020**, *132*, 4259.

[16] M. Caldarola, P. Albella, E. Cortés, M. Rahmani, T. Roschuk, G. Grinblat, R. F. Oulton, A. V. Bragas, S. A. Maier, *Nat. Commun.* **2015**, *6*, 7915.

[17] A. I. Kuznetsov, A. E. Miroshnichenko, M. L. Brongersma, Y. S. Kivshar, B. Luk'yanchuk, *Science* **2016**, *354*, 2472.

[18] C. Z. Deng, Y. L. Ho, J. K. Clark, T. Yatsui, J. J. Delaunay, *ACS Photonics* **2020**, *7*, 2915.

[19] O. E. Dagdeviren, D. Glass, R. Sapienza, E. Cortés, S. A. Maier, I. P. Parkin, P. Grütter, R. Quesada-Cabrera, *Nano Lett.* **2021**, *21*, 8348.

[20] D. Papadakis, A. Diamantopoulou, P. A. Pantazopoulos, D. Palles, E. Sakellis, N. Boukos, N. Stefanou, V. Likodimos, *Nanoscale* **2019**, *11*, 21542.

[21] X. Wang, W. Shi, S. Wang, H. Zhao, J. Lin, Z. Yang, M. Chen, L. Guo, *J. Am. Chem. Soc.* **2019**, *141*, 5856.

[22] L. Li, T. Hutter, A. S. Finnemore, F. M. Huang, J. J. Baumberg, S. R. Elliott, U. Steiner, S. Mahajan, *Nano Lett.* **2012**, *12*, 4242.

[23] D. Qi, L. Lu, L. Wang, J. Zhang, *J. Am. Chem. Soc.* **2014**, *136*, 9886.

[24] I. Alessandri, *J. Am. Chem. Soc.* **2013**, *135*, 5541.

[25] Z. Wang, C. C. Lin, Y. L. Ho, R. Xiang, S. Maruyama, C. W. Chen, J. J. Delaunay, *Adv. Opt. Mater.* **2021**, *9*, 2101474.

[26] J. Cambiasso, M. König, E. Cortés, S. Schlücker, S. A. Maier, *ACS Photonics* **2018**, *5*, 1546.

[27] S. M. Spillane, T. J. Kippenberg, K. J. Vahala, *Nature* **2002**, *415*, 621.

[28] K. Ohtaka, *J. Physical Soc. Japan* **1983**, *52*, 1457.

[29] J. M. Luther, P. K. Jain, T. Ewers, A. P. Alivisatos, *Nat. Mater.* **2011**, *10*, 361.

[30] S. Romano, G. Zito, S. Managò, G. Calafiore, E. Penzo, S. Cabrini, A. C. De Luca, V. Mocella, *J. Phys. Chem. C* **2018**, *122*, 19738.

[31] Y. T. Lin, A. Hassanfiroozi, W. R. Jiang, M. Y. Liao, W. J. Lee, P. C. Wu, *Nanophotonics* **2022**, *11*, 2701.

[32] A. Lagarkov, I. Budashov, V. Chistyaev, A. Ezhov, A. Fedyanin, A. Ivanov, I. Kurochkin, S. Kosolobov, A. Latyshev, D. Nasimov, I. Ryzhikov, M. Shcherbakov, A. Vaskin, A. K. Sarychev, *Opt. Express* **2016**, *24*, 7133.

[33] S. Jahani, Z. Jacob, *Nat. Nanotechnol.* **2016**, *11*, 23.

[34] P. Wang, A. V. Krasavin, L. Liu, Y. Jiang, Z. Li, X. Guo, L. Tong, A. V. Zayats, *Chem. Rev.* **2022**, *122*, 15031.

[35] L. Hüttenhofer, M. Golibrzuch, O. Bienek, F. J. Wendisch, R. Lin, M. Becherer, I. D. Sharp, S. A. Maier, E. Cortés, *Adv. Energy. Mater.* **2021**, *11*, 2102877.

[36] C. W. Hsu, B. Zhen, A. D. Stone, J. D. Joannopoulos, M. Soljačić, *Nat. Rev. Mater.* **2016**, *1*, 16048.

[37] K. Koshelev, S. Lepeshov, M. Liu, A. Bogdanov, Y. Kivshar, *Phys. Rev. Lett.* **2018**, *121*, 193903.

[38] A. Kodigala, T. Lepetit, Q. Gu, B. Bahari, Y. Fainman, B. Kanté, *Nature* **2017**, *541*, 196.

[39] A. Fernandez-Bravo, D. Wang, E. S. Barnard, A. Teitelboim, C. Tajon, J. Guan, G. C. Schatz, B. E. Cohen, E. M. Chan, P. J. Schuck, T. W. Odom, *Nat. Mater.* **2019**, *18*, 1172.

[40] A. Tittl, A. John-Herpin, A. Leitis, E. R. Arvelo, H. Altug, *Angew. Chem.* **2019**, *58*, 14810.

[41] A. Tittl, A. Leitis, M. Liu, F. Yesilkoy, D. Choi, D. N. Neshev, Y. S. Kivshar, H. Altug, *Science* **2018**, *1109*, 1105.

[42] W. Chen, Y. Li, Y. Liu, Y. Gao, Y. Yan, Z. Dong, J. Zhu, *Adv. Opt. Mater.* **2023**, 2301697, https://doi.org/10.1002/adom.202301697.

[43] L. Carletti, K. Koshelev, C. De Angelis, Y. Kivshar, *Phys. Rev. Lett.* **2018**, *121*, 33903.

[44] K. Koshelev, S. Kruk, E. Melik-gaykazyan, J. Choi, A. Bogdanov, H. Park, Y. Kivshar, *Science* **2020**, *367*, 288.

[45] D. Christie, J. Lombardi, I. Kretzschmar, *J. Phys. Chem. C* **2014**, *118*, 9114.

[46] S. A. Dyakov, M. V. Stepikhova, A. A. Bogdanov, A. V. Novikov, D. V. Yurasov, M. V. Shaleev, Z. F. Krasilnik, S. G. Tikhodeev, N. A. Gippius, *Laser Photon. Rev.* **2021**, *15*, 2000242.

[47] A. S. Kupriianov, Y. Xu, A. Sayanskiy, V. Dmitriev, Y. S. Kivshar, V. R. Tuz, *Phys. Rev. Appl.* **2019**, *12*, 014024.

[48] Y. Ra'Di, A. Krasnok, A. Alù, *ACS Photonics* **2020**, *7*, 1468.

[49] S. E. J. Bell, G. Charron, E. Cortés, J. Kneipp, M. L. de la Chapelle, J. Langer, M. Procházka, V. Tran, S. Schlücker, *Angew. Chem.* **2020**, *59*, 201908154.

[50] S. Fan, W. Suh, J. D. Joannopoulos, *JOSA A* **2003**, *20*, 569.

[51] S. A. Maier, *Opt. Express* **2006**, *14*, 1957.

[52] J. Zhao, H. Lui, D. I. Mclean, H. Zeng, *Appl. Spectrosc.* **2007**, *61*, 1225.

[53] D. Rustichelli, S. Castiglia, M. Gunetti, K. Mareschi, E. Signorino, M. Muraro, L. Castello, F. Sanavio, M. Leone, I. Ferrero, F. Fagioli, *J. Transl. Med.* **2013**, *11*, 197.

[54] V. Burtsev, M. Erzina, O. Guselnikova, E. Miliutina, Y. Kalachyova, V. Svorcik, O. Lyutakov, *Analyst* **2021**, *146*, 3686.

[55] G. Song, W. Gong, S. Cong, Z. Zhao, *Angew. Chem.* **2021**, *60*, 5505.

[56] X. Wang, W. Shi, G. She, L. Mu, *J. Am. Chem. Soc.* **2011**, *133*, 16518.

[57] J. R. Lombardi, R. L. Birke, *J. Phys. Chem. C* **2014**, *118*, 11120.

[58] H. Hu, T. Weber, O. Bienek, A. Wester, L. Hüttenhofer, I. D. Sharp, S. A. Maier, A. Tittl, E. Cortés, *ACS Nano* **2022**, *16*, 13057.

[59] S. Y. Ding, E. M. You, Z. Q. Tian, M. Moskovits, *Chem. Soc. Rev.* **2017**, *46*, 4042.

[60] M. R. Hasan, O. G. Helleso, *Opt. Express* **2023**, *31*, 6782.

[61] P. T. Kristensen, C. Van Vlack, S. Hughes, *Opt. Lett.* **2012**, *37*, 1649.

[62] E. A. Muljarov, W. Langbein, *Phys. Rev. B* **2016**, *94*, 235438.

[63] A. E. Krasnok, A. P. Slobozhanyuk, C. R. Simovski, et al., *Sci. Rep.* **2015**, *5*, 12956.

[64] F. Laux, N. Bonod, D. Gérard, *J. Phys. Chem. C* **2017**, *5*, 12956.